Simulation of cemented granular materials. I. Macroscopic stress-strain response and strain localization

Nicolas Estrada* and Arcesio Lizcano
Departamento de Ingeniería Civil y Ambiental–CeiBA Complex Systems Research Center, Universidad de Los Andes, Bogotá, Colombia

Alfredo Taboada
Laboratoire Géosciences Montpellier, Université de Montpellier II–CNRS, Montpellier, France
(Received 11 February 2010; published 23 July 2010)

This is the first of two papers investigating the mechanical response of cemented granular materials by means of contact dynamics simulations. In this paper, a two-dimensional polydisperse sample with high-void ratio is constructed and then sheared in a simple shear numerical device at different confinement levels. We study the macroscopic response of the material in terms of mean and deviatoric stresses and strains. We show that the introduction of a local force scale, i.e., the tensile strength of the cemented bonds, causes the material to behave in a rigid-plastic fashion, so that a yield surface can be easily determined. This yield surface has a concave-down shape in the mean:deviatoric stress plane and it approaches a straight line, i.e., a Coulomb strength envelope, in the limit of a very dense granular material. Beyond yielding, the cemented structure gradually degrades until the material eventually behaves as a cohesionless granular material. Strain localization is also investigated, showing that the strains concentrate in a shear band whose thickness increases with the confining stress. The void ratio inside the shear band at the steady state is shown to be a material property that depends only on contact parameters.

DOI: 10.1103/PhysRevE.82.011303 PACS number(s): 81.05.Rm, 83.80.Nb, 91.60.Ba

I. INTRODUCTION

Cementation, a common property among geomaterials, often results from the precipitation of minerals such as clay, calcium carbonate, and iron oxides at the contacts between grains [1]. Examples of cemented geomaterials frequently encountered in nature are volcanic ash soils and sandstones.

The effect of cementation on the stress-strain response of soils and rocks is of special interest in fields such as geotechnical engineering and geology, frequently concerned about the stability of structures such as road slopes and foundations. However, the mechanical behavior of cemented geomaterials differs from that observed in cohesionless soils, for which classical soil mechanics was developed [2–6]. In particular, the behavior of cemented geomaterials changes drastically if a certain "yield" stress is attained. Beyond this yield stress, the material begins to "destructurate" and its behavior gradually approaches that of a cohesionless soil. Two main features control yielding in cemented geomaterials: (1) the magnitude of the local force scale introduced by cementation, i.e., the tensile strength of the cemented bonds; and (2) the peculiar geometrical arrangement of grains (microstructure) that can be achieved because of local adhesion; e.g., it is common to find cemented soils in much looser states than those that can be reached by a cohesionless granular material, regardless of the preparation method.

Some constitutive models have been developed which introduce the effect of cementation at the scale of a representative elementary volume [7–9]. Most of them are extensions of the elastoplastic models proposed for clays since 40 years ago [10,11]. These models can be implemented in a finite element framework and succeed to reproduce the major trends of the macroscopic behavior observed in laboratory experiments. This "continuum" approach is thus useful when applied to some practical engineering problems. However, it often involves parameters that cannot be clearly related to local interactions, grain characteristics, or microstructure; and it is based on experimental measurements that are difficult to obtain, e.g., the yield surface.

On the other hand, discrete element simulations provide a suitable tool to investigate the behavior of model granular materials, drawing connections between the local and global scales. Some works with discrete element methods have been devoted to the behavior of partially saturated granular materials, in which cohesion between grains results from capillarity [12–14]. Are also to be mentioned some numerical investigations on the mechanical response of cohesive powders, in which the cohesive interactions are due to van der Waals forces (see, for example [15,16], and references therein). However, few numerical studies using discrete element methods have been devoted to the behavior of cemented granular materials [17–21].

The aim of this work is to investigate the strength and strain properties of a two-dimensional cemented granular material sheared in a simple shear numerical device. The idea is to determine the yield surface and to study strain localization in this simplified system. Our results provide insights on the behavior of cemented granular materials, guiding various modeling choices such as the shape of the yield surface, the direction of the plastic strains at yielding, and the thickness of the shear band. Alternatively, the macroscopic description of the system is an obliged step before studying the role played by local interactions, particle characteristics, and micro-structure on the global mechanical response of the material; this issue is treated in the companion paper, hereafter referred as paper II.

*n.estrada22@uniandes.edu.co

We first present the numerical method as well as the model of cementation in Sec. II. In Sec. III, we describe the method used to construct the granular samples and the device used to investigate their mechanical response, i.e., the simple shear numerical device. In Sec. IV, we present our results focusing on the initial yielding of the material, its behavior at the steady state, and strain localization. Finally, in Sec. V, we conclude with a summary of the main results and a brief discussion.

II. CONTACT DYNAMICS-CEMENTATION MODEL

The simulations presented in this paper were carried out using the contact dynamics method, which is suitable for simulating large assemblies of rigid particles [22–26]. This method has been widely applied to simulate cohesionless materials with frictional interactions at their contacts. In order to simulate cemented granular materials, two additional elements must be introduced: tensile strength and torque transmission at the contacts. In the following subsections, we present a brief description of the method for frictional cohesionless disks as well as the modifications that must be implemented in order to introduce these two new elements.

A. Contact dynamics method for frictional cohesionless materials

The contact dynamics method can be seen as the combination of three main ingredients. The first ingredient are the equations of motion for each particle, which, integrated over a small time step Δt, relate the impulsion to the change of momentum of each particle over the time step. These equations can be written as

$$\Delta t\left(\sum_{c\in p}\boldsymbol{f}^c + m\boldsymbol{g}\right) = m\Delta\boldsymbol{v}^p,$$

$$\Delta t\left(\sum_{c\in p}\boldsymbol{f}^c \times \boldsymbol{r}^c\right) = I\Delta\boldsymbol{w}^p, \tag{1}$$

where $\boldsymbol{f}^c$ is the force exerted on particle p at contact c, m is the mass of the particle, $\boldsymbol{g}$ is the gravity (which is set to zero for all the simulations presented in this paper and in paper II), $\Delta\boldsymbol{v}^p$ is the change of velocity of the particle during the time step, $\boldsymbol{r}^c$ is the position vector of the contact, I is the moment of inertia of the particle, $\Delta\boldsymbol{w}^p$ is the change of angular velocity of the particle during the time step, and the summations run over all the contacts c on particle p.

The second ingredient of the method is a set of contact laws, which relate the impulsions exerted at each contact with the change of relative velocity during the time step. The method supposes that grains are perfectly rigid, and the usual contact laws are perfect volume exclusion and Coulomb friction. At a given instant, these two laws can be expressed as complementary relations between the forces and the relative velocities at the contacts. In the normal direction, the condition of impenetrability of the grains at a contact (i.e., when the gap $\delta=0$) implies the following complementary relation:

$$u_n = 0 \Rightarrow f_n \geq 0,$$

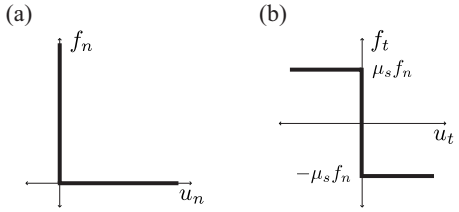

FIG. 1. (a) Signorini's condition relating the normal force f_n and the relative normal velocity u_n at a contact. (b) Coulomb friction law relating the tangential force f_t and the relative tangential velocity u_t at a contact.

$$u_n > 0 \Rightarrow f_n = 0, \tag{2}$$

where u_n is the relative normal velocity at the contact and f_n is the normal component of the contact force (we attribute positive values to compressive forces and diverging relative normal velocities). This relation, called the Signorini's condition for velocities, is shown as a graph in Fig. 1(a). In the tangential direction, the Coulomb friction law can be described by the following complementary relation:

$$u_t > 0 \Rightarrow f_t = -\mu_s f_n,$$

$$u_t = 0 \Rightarrow -\mu_s f_n \leq f_t \leq \mu_s f_n,$$

$$u_t < 0 \Rightarrow f_t = \mu_s f_n, \tag{3}$$

where u_t is the sliding velocity at the contact, f_t is the tangential component of the contact force (i.e., the friction force), and μ_s is the coefficient of sliding friction. Figure 1(b) shows the Coulomb friction law as a graph.

At the scale of a time step, the formulation of the contact laws involves two coefficients of restitution (normal and tangential) controlling the amount of energy dissipated during collisions. In all the simulations presented in this paper and in paper II, the coefficients of restitution are set to zero. In fact, it has been shown using numerical simulations [32] that the quasistatic behavior of sheared granular systems is almost independent of the coefficient of restitution unless this parameter is set to very large values (say over 0.8).

Note that the contact laws are *nonsmooth* in the sense that they cannot be reduced to (mono)valued functional dependences between the impulsions and the change of relative velocities at the contacts. Instead, these contact laws are described as complementary relations between these two quantities, avoiding the introduction of regularization or damping parameters. This fundamental ingredient is an advantage of the method, since it allows the utilization of bigger time steps and greater numbers of grains in comparison with other discrete element methods.

The third ingredient of the method is an algorithm of solution. The system of equations to be solved is of implicit type, since, strictly speaking, the solution for a given grain depends on the solutions for all the grains in the system in the same time step. The impulsions and changes of momentum of each grain are thus determined using an iterative al-

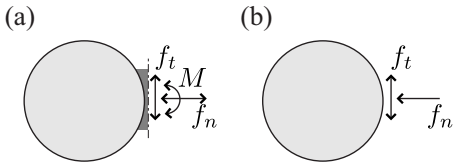

FIG. 2. Schematic representation of the cementation model. (a) Intact cemented bonds support tensile forces, shear forces, and torques. (b) Post-rupture contacts are only frictional.

gorithm similar to a Gauss-Seidel scheme. For specific implementation of the contact dynamics method for cohesionless frictional materials see [26,27].

B. Cementation model

Our cementation model considers that intact cemented bonds resist, up to certain thresholds, tensile forces, shear forces, and torques. The rupture of a bond leads to an irreversible loss of tensile strength and torque transmission, and the contact turns to purely frictional behavior; see Fig. 2.

In the following subsections, we present the implemented contact laws accounting for tensile strength and torque transmission. Subsequently, we introduce the contact parameters that control the kinetics of bond creation and rupture.

1. Tensile and shear strength

We consider that bond rupture along the normal direction is controlled by the force threshold f_a, which represents the largest tensile force that can be supported by a cemented bond. The force threshold f_a is given by

$$f_a = h\ell\sigma_a, \tag{4}$$

where h is the width of the cemented bond normalized by the mean diameter ℓ of the two grains in contact, and σ_a is the tensile strength of the cementing material.

Tensile strength is easily introduced in the contact dynamics method by shifting downwards the Signorini's condition [see Fig. 3(a)], so that the complementary relations 2 and 3 must be modified as follows:

$$u_n = 0 \Rightarrow f_n \geq -f_a,$$

$$u_n > 0 \Rightarrow f_n = -f_a, \tag{5}$$

and

$$u_t > 0 \Rightarrow f_t = -\mu_s(f_a + f_n),$$

$$u_t = 0 \Rightarrow -\mu_s(f_a + f_n) \leq f_t \leq \mu_s(f_a + f_n),$$

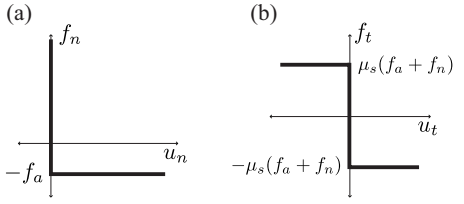

FIG. 3. (a) Signorini's condition for a cemented bond. (b) Coulomb friction law for a cemented bond.

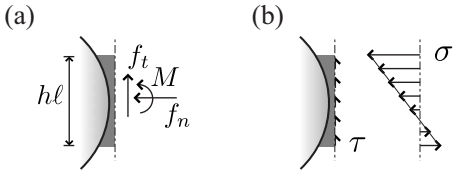

FIG. 4. (a) Cemented bond bearing a normal force f_n, a tangential force f_t, and a torque M. (b) Normal σ and tangential τ stress distributions in the cemented bond.

$$u_t < 0 \Rightarrow f_t = \mu_s(f_a + f_n). \tag{6}$$

The Coulomb friction law for a cemented bond is shown as a graph in Fig. 3(b).

2. Torque transmission

Torque transmission results from the nonuniform distribution of normal stresses in a cemented bond, which exerts a torque around the middle contact point between two grains. In our model, we assume that the contact torque M transmitted by a cemented bond cannot exceed a threshold M_{max}. This threshold is reached when the maximum tensile stress in the bond equals the tensile strength σ_a. For example, for a linear stress distribution (see Fig. 4), the maximum torque M_{max} that can be supported by a cemented bond is given by

$$M_{max} = \frac{(h\ell)^2}{6}(\langle\sigma\rangle + \sigma_a) = \frac{h\ell}{6}(f_n + f_a), \tag{7}$$

where $\langle\sigma\rangle = f_n/(h\ell)$ is the mean normal stress in the bond.

In the contact dynamics method, torque transmission can be introduced through a "rolling resistance" law analogous to the Coulomb friction law. The rolling resistance law relates the torque M to the relative angular velocity $\omega_r = \omega_i - \omega_j$, where ω_i and ω_j are the angular velocities of the two grains, i and j, in contact. This law can be described by the following complementary relation:

$$\omega_r > 0 \Rightarrow M = -\mu_r\ell(f_a + f_n),$$

$$\omega_r = 0 \Rightarrow -\mu_r\ell(f_a + f_n) \leq M \leq \mu_r\ell(f_a + f_n),$$

$$\omega_r < 0 \Rightarrow M = \mu_r\ell(f_a + f_n), \tag{8}$$

where μ_r is the coefficient of rolling friction, and the scaling of the rolling threshold with ℓ is meant to make μ_r dimensionless. Figure 5 shows the rolling resistance contact law as a graph.

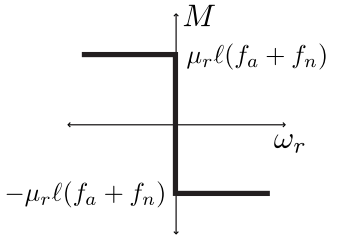

FIG. 5. Rolling resistance contact law, relating the torque M and the relative angular velocity ω_r at a contact between two grains.

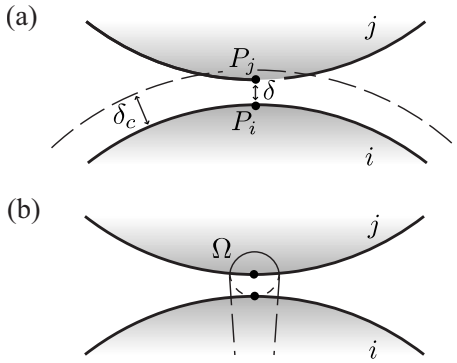

FIG. 6. Kinetics of bond creation and rupture: (a) creation length δ_c and (b) circular zone Ω controlling bond rupture.

3. Kinetics of bond creation and rupture

Our cementation model considers that the kinetics of bond creation and rupture is governed, respectively, by a creation length δ_c and a circular zone Ω of weak extension located between the grains (Fig. 6). The first condition allows for the creation of cemented bonds between particles such that the gap δ, i.e., the distance between their two closest material points P_i and P_j, is below δ_c. This is also observed in real cemented geomaterials, since minerals can precipitate in the interstice between two particles if the gap between them is small enough. The second condition states that a cemented bond persists as long as the point P_j remains inside a small circular zone Ω fixed to disk i. Once the point P_j exits Ω, the cemented bond is considered to be broken. This small zone represents in a way the local strain associated to the rupture of a cemented bond. The parameter δ_c and the size of the circular zone Ω are small compared to the average diameter of the disks in contact (i.e., δ_c and $\Omega=0.005\ell$). These parameters simply control the "brittleness" of the material, and they do not influence the results presented in this paper.

III. SIMULATIONS

A. Sample construction

The purpose of the sample construction procedure is to construct fully cemented loose arrangements of grains. For this reason, all contacts created during this procedure are considered to be cohesive with a tensile threshold $f_a=3\ell$ kPa, a coefficient of sliding friction $\mu_s=0.3$, and a coefficient of rolling friction $\mu_r=0$. As explained in Sec. III B, once the construction procedure has been completed, new contact parameters reflecting the behavior of cemented bonds are assigned to the sample. In particular, a coefficient of rolling friction is assigned to the cemented bonds during the shear test. The introduction of this parameter strongly increases the strength of the system. In the following, we present the two phases of the sample construction procedure, termed as *aggregation* and *densification*.

1. Aggregation

Our numerical samples are composed of 10 000 disks with diameters uniformly distributed between $0.4\langle d\rangle$ and $1.6\langle d\rangle$, where $\langle d\rangle=0.01$ m is the mean diameter. The grains are randomly placed in the nodes of a square grid of 100×100 elements. The length of the grid elements is $1.6\langle d\rangle$; thus, at the beginning of the aggregation phase, the grains do not overlap. The sample is placed inside a semiperiodic square box, and a random velocity between 0 and 0.01 m/s is assigned to each grain. Next, the grains gradually aggregate forming cohesive clusters, until their velocity finally vanishes as a result of inelastic collisions. Figure 7 shows two snapshots of the sample at the beginning and at the end of the aggregation phase.

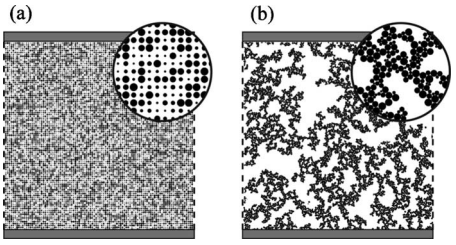

FIG. 7. Snapshots of the sample and zooms of a portion of the sample at (a) the beginning and (b) the end of the aggregation phase.

2. Densification

After the aggregation phase, the samples are densified by applying a vertical stress σ_{wall} to the upper wall. This induces the downward displacement of the wall until the stress σ_{wall} is finally equilibrated by the contact forces.

It is convenient to quantify the relative importance of the imposed stress by means of a dimensionless parameter comparing σ_{wall} to the local stress scale. To do so, let us introduce the dimensionless vertical stress σ^*_{wall} given by

$$\sigma^*_{wall}=\frac{\sigma_{wall}}{\langle f_a\rangle/\langle d\rangle}=\frac{\sigma_{wall}}{h\sigma_a}, \tag{9}$$

where $\langle f_a\rangle$ is the largest tensile force that can be supported by a cemented bond between two grains of mean diameter $\langle d\rangle$.

The compactness of the sample at the end of the densification phase can be represented by the void ratio e defined by

$$e=\frac{V_v}{V_p}, \tag{10}$$

where V_v is the volume occupied by the voids and V_p is the volume occupied by the particles. The void ratio e is related to the solid fraction ν by the simple expression $e=(1/\nu)-1$.

Figure 8 shows the void ratio at the end of the densification phase as a function of the dimensionless vertical stress σ^*_{wall}. The dashed line represents the void ratio obtained for a reference cohesionless material (i.e., with the same polydispersity and the same sliding friction coefficient) densified with this procedure. The polar distribution of contact orientations for three of the obtained samples is also displayed in Fig. 8, showing that they are almost isotropic.

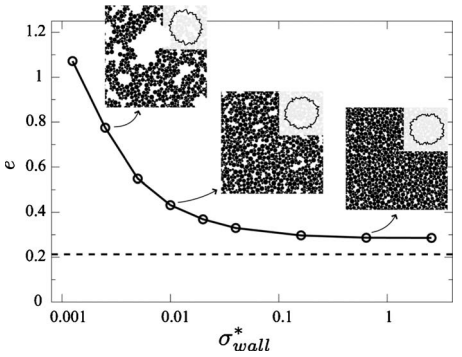

FIG. 8. Void ratio e at the end of the densification phase as a function of the dimensionless vertical stress σ^*_{wall}. A portion of the sample and the polar distribution of contact orientations are also displayed for three of the obtained samples.

B. Simple shear test

Once constructed, the samples are sheared in a simple shear numerical device in a two-phase procedure. These phases are termed as *confinement* and *shear*.

Table I shows the contact parameters used during the simple shear test. The *initial* parameters are assigned to all the contacts at the beginning of the test, while the *residual* parameters are assigned to the broken bonds and to the new contacts created during the test. Note that this set of parameters mimics cementation, since all contacts at the beginning of the shear test resist tensile forces and torques, while their post-rupture behavior is only frictional.

1. Confinement

First, a vertical stress σ_{wall} is applied to the upper wall. As it will be shown in Sec. IV A 2, in a loose sample, the vertical stress σ_{wall} may be strong enough to break some cemented bonds inducing considerable deformations in the sample.

2. Shear

Second, the sample is sheared by imposing to the upper wall a horizontal velocity v_{wall} while maintaining the vertical stress σ_{wall}; see Fig. 9. To avoid strain localization along the boundaries, relative movement between the walls and the grains in contact with them is inhibited. The samples are sheared at different dimensionless vertical stresses σ^*_{wall} up to a large cumulative shear strain $\gamma = x_{wall}/y_{wall} \simeq 2.5$, where

TABLE I. Contact parameters during simple shear test. The *initial* parameters are assigned to all the contacts at the beginning of the test, while the *residual* parameters are assigned to the broken bonds and to the new contacts created during the test.

Parameter	Initial behavior	Residual behavior
h	0.1	0
σ_a	30 kPa	0
μ_s	0.3	0.3
μ_r	0.0167	0

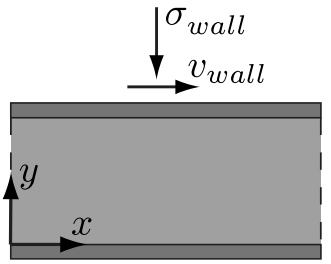

FIG. 9. Schematic representation of the simple shear test. The dashed lines represent periodic boundaries.

x_{wall} is the horizontal displacement of the upper wall and y_{wall} is its vertical position. This allows to study the behavior of the material in the initial and steady states.

IV. RESULTS

In this section, we first identify the stress states at which the undamaged cemented system initially yields (Sec. IV A). For this purpose, we analyze the system at the confining phase and at the beginning of the shear phase at low confinement levels (i.e., at confining stresses that did not damage the system during the confinement phase). Then, in Sec. IV B, we study the mechanical response of the material as it is sheared, at both low and high confining levels, until it eventually reaches the steady state characterized by constant void ratio and shear strength. All results presented in Secs. IV A and IV B were obtained using only one of the samples constructed with the procedure described in Sec. III A; this is, the sample densified with a dimensionless vertical stress $\sigma^*_{wall}=0.01$. Finally, in Sec. IV C, we investigate the effect of the initial compactness of the system on the shape of the yield surface.

A. Initial yielding

1. Macroscopic stresses and strains

Let us introduce the dimensionless mean and deviatoric stresses, p^* and q^*, respectively defined as

$$p^* = \frac{\sigma_1 + \sigma_3}{2h\sigma_a}, \quad q^* = \frac{\sigma_1 - \sigma_3}{2h\sigma_a}, \tag{11}$$

where σ_1 and σ_3 are, respectively, the major and minor principal stresses, i.e., the eigenvalues of the stress tensor $\boldsymbol{\sigma}$. The stress tensor can be calculated at any stage of the simulation from particles' positions and contact forces. We first compute the internal moment tensor $\boldsymbol{M}^p$ of each grain defined by [28,29]

$$M^p_{\alpha\beta} = \sum_{c \in p} f^c_\alpha r^c_\beta, \tag{12}$$

where α and β represent the components in an orthonormal reference frame. The average stress tensor $\boldsymbol{\sigma}$ in a volume V of the granular assembly is given by

$$\sigma_{\alpha\beta} = \frac{1}{V} \sum_{p \in V} M^p_{\alpha\beta}. \tag{13}$$

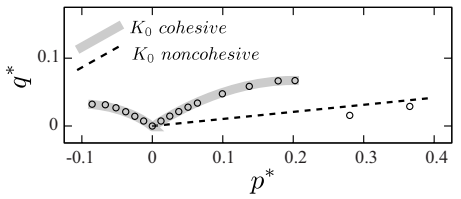

FIG. 10. Dimensionless mean p^* and deviatoric q^* stresses at the end of the confinement phase for 18 different dimensionless vertical stresses σ^*_{wall} ranging from −0.12 to 0.4. This is known as the K_0 compression trajectory in soil mechanics. The dashed line represents the K_0 trajectory for the reference cohesionless material.

The volumetric and deviatoric strains, ε_p and ε_q, respectively, are given by

$$\varepsilon_p = \varepsilon_1 + \varepsilon_3, \quad \varepsilon_q = \varepsilon_1 - \varepsilon_3, \tag{14}$$

where ε_1 and ε_3 are, respectively, the major and minor principal strains, which at small strains are given by

$$\varepsilon_1, \varepsilon_3 = \frac{\varepsilon_{xx} + \varepsilon_{yy}}{2} \pm \sqrt{\left(\frac{\varepsilon_{xx} - \varepsilon_{yy}}{2}\right)^2 + \left(\frac{\gamma}{2}\right)^2}, \tag{15}$$

where ε_{xx} and ε_{yy} are, respectively, the strains in the x and y directions.

2. Confinement phase

Figure 10 shows the dimensionless mean p^* and deviatoric q^* stresses measured in the sample at the end of the confinement phase for 18 different dimensionless vertical stresses σ^*_{wall} ranging from −0.12 to 0.4. This is known as the K_0 compression trajectory in soil mechanics. The dashed line represents the K_0 trajectory for the reference cohesionless material (please note that both axes in Fig. 10 are normalized by $h\sigma_a$, which is not defined in the cohesionless system; however, since both axes are normalized by the same value, the slope of the dashed line remains unchanged). As observed in laboratory experiments [4,5], two types of behavior can be identified. Below a certain value of mean stress (i.e., $p^* \lesssim 0.2$) the K_0 trajectory for the cemented material is a curve line. For higher mean stresses, the K_0 trajectory of the cemented material falls close to that of the reference cohesionless material, showing that the dimensionless vertical stress σ^*_{wall} is strong enough to damage the cemented structure inducing a significant compaction of the sample. The transition between these two types of behavior, controlled by the stress level imposed to the sample (i.e., by σ^*_{wall}), is a macroscopic manifestation of the local force scale introduced by the tensile strength f_a.

3. Shear phase

Figure 11 shows stress-strain and volumetric strain plots for the sample sheared at four different dimensionless vertical stresses (σ^*_{wall}: −0.1, 0, 0.1, and 0.2). The dimensionless mean stress p^* [Fig. 11(a)] remains almost constant during shearing, as it is expected in a simple shear test. On the other hand, the dimensionless deviatoric stress q^* [Fig. 11(b)] rises to a peak in a rigid fashion and then, after a short plateau,

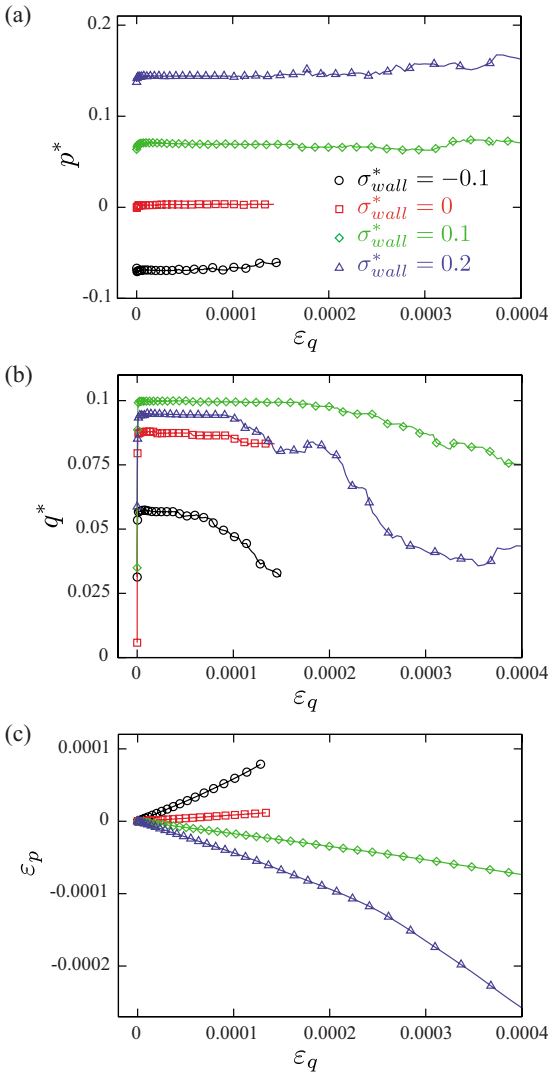

FIG. 11. (Color online) Stress-strain response of the material at the beginning of the shear phase: (a) dimensionless mean stress p^*, (b) dimensionless deviatoric stress q^*, and (c) volumetric strain ε_p, as functions of the deviatoric strain ε_q.

decreases with the deviatoric strain ε_q. This happens because in any of these four tests the cemented structure was damaged during the confinement phase; as it will be shown in Sec. IV B 1, if the cemented structure is damaged during the confinement phase, the material behaves as a loose cohesionless granular material.

Figure 11(c) shows the volumetric strain ε_p in the four tests, showing that in the tests performed at low vertical stresses (i.e., for σ^*_{wall}: −0.1 and 0) the sample dilates, while in the tests performed at high-vertical stresses (i.e., for σ^*_{wall}: 0.1 and 0.2) the sample contracts. Once again, the influence of the confinement level on the behavior of the material results from changing the relative importance of the local force scale when compared to the external forces applied to the system.

4. Yield surface and plastic strain vectors

Since the particles are perfectly rigid, the peak strength and the plastic strains displayed in Fig. 11 can be considered

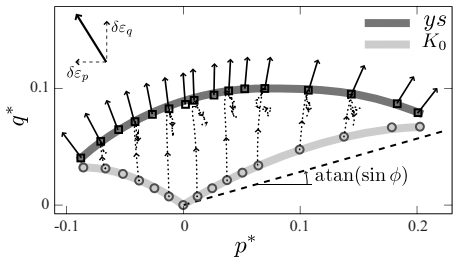

FIG. 12. Stress paths (dotted lines) in the $(p^*:q^*)$ stress plane followed in eight tests performed at different dimensionless vertical stresses σ^*_{wall}. The dark gray stripe represents the yield surface *ys*, the light gray stripe represents the K_0 compression trajectory, the dashed line represents the Coulomb strength envelope for the reference cohesionless material at the steady state, and the arrows represent the plastic strain vectors, following the convention shown in the inset.

as the yield stresses and strains. The dotted lines in Fig. 12 display the stress paths followed in eight tests performed at different dimensionless vertical stresses σ^*_{wall}; as it was shown in Fig. 11(b) the deviatoric stress rises to a peak and then decreases. The line joining these peaks (i.e., the yield stress states) defines the yield surface (dark gray stripe in Fig. 12) of the material in the $(p^*:q^*)$ stress plane. The dashed line represents the Coulomb strength envelope for the reference cohesionless material in the steady state, characterized by the angle of internal friction ϕ. It can be seen that the yield surface has a concave-down shape, as observed in laboratory experiments with clays and cohesive soils.

The vectors drawn in each yield point in Fig. 12 represent the direction of the incremental plastic strains, $\delta\varepsilon_p$ and $\delta\varepsilon_q$, at yielding, following the convention shown in the inset. Once again, it can be seen that the sample exhibits a dilatant behavior (plastic strain vectors inclined to the left) at low mean stress levels (i.e., $p^* \lesssim 0.02$) and a contractant behavior (plastic vectors inclined to the right) at high-mean stress levels. Remark that the yield surface and the plastic strain vectors can be easily determined from simulation data, in contrast to laboratory experiments with intact real materials, in which they are often difficult to obtain.

B. Steady state

1. Stress-strain response

Figure 13 shows stress-strain and normalized volume plots for the sample sheared up to the steady state at four different dimensionless vertical stresses (σ^*_{wall}:0.02, 0.08, 0.15, and 0.3).

As mentioned earlier, the dimensionless mean stress p^* remains almost constant during the test; see Fig. 13(a). On the other hand, the dimensionless deviatoric stress q^* [Fig. 13(b)] shows two types of behavior, depending on whether or not the dimensionless vertical stress σ^*_{wall} is strong enough to damage the cemented structure during the confinement phase. If the sample is not damaged during the confinement phase (i.e., for σ^*_{wall}:0.02 0.08, and 0.15), the dimensionless deviatoric stress initially rises to a peak, then declines abruptly, and then increases to a value of residual strength

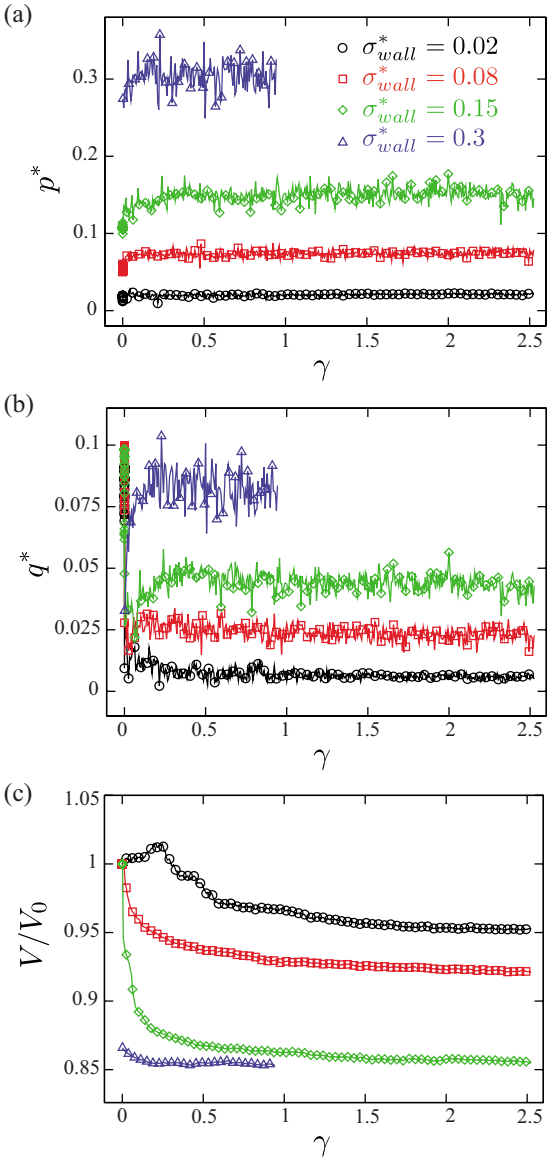

FIG. 13. (Color online) Stress-strain response of the sample sheared up to the steady state: (a) dimensionless mean stress p^*, (b) dimensionless deviatoric stress q^*, and (c) normalized volume V/V_0, where V_0 is the initial volume of the packing, as functions of the cumulative shear strain γ.

which eventually stabilizes as the shear strain γ increases. On the other hand, if the sample is damaged during the confinement phase (i.e., for σ^*_{wall}:0.3), the dimensionless deviatoric stress q^* shows no initial peak, but it increases with γ and then stabilizes as observed in loose cohesionless granular materials.

The steady state is approached as the cemented bonds gradually break inducing the contraction of the sample, even for those tests that initially showed a dilatant behavior; see Fig. 13(c). After sufficiently large shearing, the volume of the sample eventually stabilizes indicating that the steady state has been reached. Note that the volume of the sample at the steady state is larger in the tests performed with low vertical stresses. However, it has been shown that the compactness of the material at the steady state is a material prop-

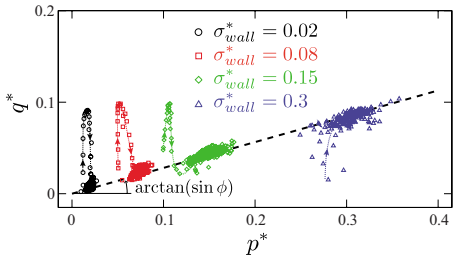

FIG. 14. (Color online) Stress paths followed in four tests performed at four different dimensionless vertical stresses σ^*_{wall}. The dashed line represents the Coulomb strength envelope for the reference cohesionless material in the steady state.

erty independent of the stress level [30,31]. Thus, the differences in the volume of the sample at the steady state observed in our tests suggest that the strains are not homogeneously distributed in the sample. This aspect is treated in Sec. IV B 2.

Figure 14 shows the stress paths followed in the four tests presented in Fig. 13. The dashed line represents the Coulomb strength envelope for the reference cohesionless material in the steady state. This figure shows that, as the cemented structure is gradually damaged, the behavior of the cemented material approaches that of the reference cohesionless granular material in the steady state.

2. Strain localization

Figure 15 shows the normalized profiles of the average horizontal displacement $\langle x\rangle/x_{wall}$ of the particles versus their vertical position y/y_{wall} at the end of the tests for the four shear tests presented in Figs. 13 and 14. These profiles evidence a different deformation pattern depending on the dimensionless vertical stress σ^*_{wall} applied to the sample. In the tests performed at low-vertical stresses (i.e., for σ^*_{wall}:0.02 and 0.08) the strain concentrates in a narrow shear band, while in the tests performed at high vertical stresses (i.e., for σ^*_{wall}:0.15 and 0.3) the strain is homogeneously distributed within the sample. Figure 16 shows the thickness H of the

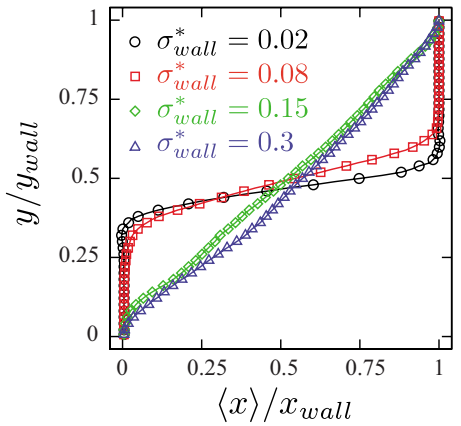

FIG. 15. (Color online) Normalized profiles of the average horizontal displacement $\langle x\rangle/x_{wall}$ of the particles versus their vertical position y/y_{wall} in the sample sheared up to the steady state at four different dimensionless vertical stresses σ^*_{wall}.

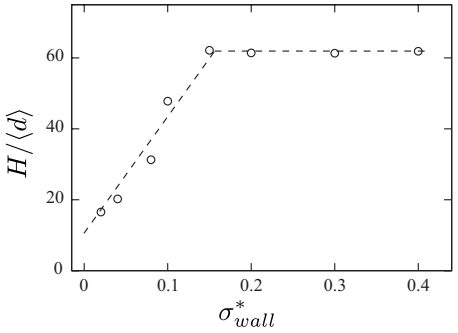

FIG. 16. Normalized thickness of the shear band $H/\langle d\rangle$ as a function of the dimensionless vertical stress σ^*_{wall}. The dashed lines are guides to the eyes.

shear band normalized by the mean diameter $\langle d\rangle$ as a function of the dimensionless vertical stress σ^*_{wall} for eight tests. This figure shows that the thickness of the shear band increases linearly with the vertical stress from a minimum value of approximately $10\langle d\rangle$ for $\sigma^*_{wall}\simeq 0$ until it eventually attains the thickness of the sample ($\simeq 60\langle d\rangle$). This behavior is probably related to an increasing capability to "damage" the cemented bonds located in the vicinity of the shear band, linked to the magnitude of the stress fluctuations in the steady state. As shown in Fig. 13, these stress fluctuations increase with the stress level applied to the sample.

We can now verify if the compactness of the granular material in the steady state depends on the confinement level applied to the sample. Figure 17 displays the void ratio e inside the shear band as a function of the cumulative shear strain γ for the four tests presented in Figs. 13–15. The dashed line represents the void ratio of the reference cohesionless material in the steady state. As expected, the void ratio in the shear band at the steady state is the same for the four tests, showing that this limit void ratio is a material property that only depends on the contact parameters.

Once the thickness of the shear band is known, we can also evaluate the average level of inertia in our simple shear tests by evaluating the inertia parameter I defined as [32]

$$I = \frac{\dot{\gamma}\langle d\rangle}{\sqrt{\sigma_{wall}/\rho}}, \tag{16}$$

where $\dot{\gamma}=v_{wall}/H$ is the shear rate and ρ is the density of the particles. A sheared system is in a quasistatic state if $I \ll 1$. In

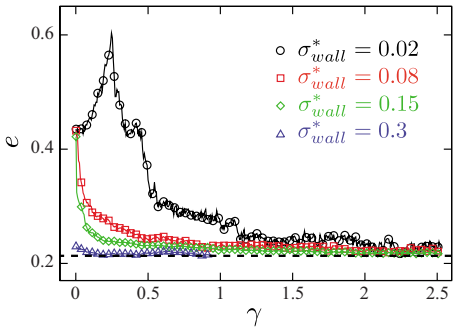

FIG. 17. (Color online) Void ratio e inside the shear band as a function of the cumulative shear strain γ, for four tests performed at different dimensionless vertical stresses σ^*_{wall}.

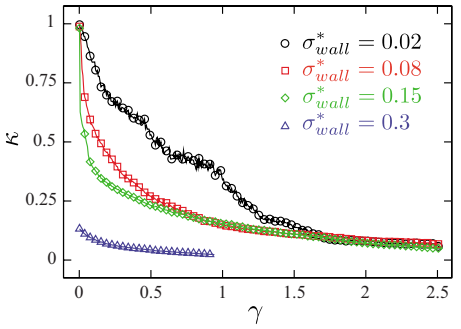

FIG. 18. (Color online) Proportion κ of cemented contacts inside the shear band as a function of the cumulative shear strain γ, for four tests performed at different dimensionless vertical stresses σ^*_{wall}.

all our tests we have $v_{wall}=(10^{-2}/\langle d\rangle)\sqrt{\sigma_{wall}/\rho}$. Thus, I ranges from $I=6\times10^{-4}$ for the tests performed at low vertical stresses (i.e., $\sigma^*_{wall}=0$, 02) to $I=1$, 6×10^{-4} for the test performed at high vertical stress (i.e., $\sigma^*_{wall}=0$, 4), meaning that our samples can reasonably be considered to be sheared in a quasistatic regime.

3. Degradation of the cemented structure

An important feature for the conception and calibration of constitutive models is how the cemented structure gradually degrades as the material is deformed. While this is hardly measurable in a real cemented soil, it can be easily obtained from simulation data and represented by the proportion κ of cemented contacts inside the shear band. Figure 18 shows the proportion κ as a function of the cumulative shear strain γ. It can be seen that κ decays with the shear strain and eventually vanishes in the steady state. The decay rate increases with the dimensionless vertical stress σ^*_{wall}, as a result of increasing contact forces.

C. Effect of the initial compactness on the shape of the yield surface

An interesting question is how the shape of the yield surface depends on the initial compactness of the cemented material. Let us thus consider the set of samples constructed in Sec. III A. The difference between these samples is their void ratio. Figure 19 shows a set of yield surfaces, each of them corresponding to one of these samples. For loose

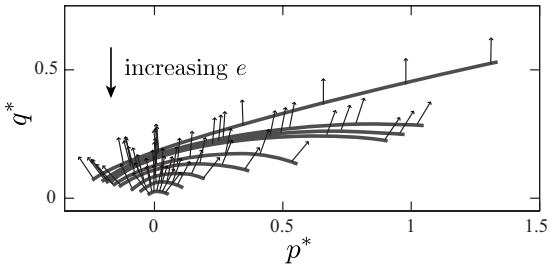

FIG. 19. Set of yield surfaces and plastic strain vectors obtained for nine samples with different void ratios e:0.213, 0.286, 0.287, 0.297, 0.330, 0432, 0.549, and 0.775.

samples, i.e., for high values of e, the yield surface is a small concave-down curve. In contrast, as e decreases, the yield surface gradually grows approaching a straight line shifted upward in the $(p^*:q^*)$ stress plane. This shows that the initial compactness of the material, here represented by the void ratio e, controls a smooth transition between two limit shapes of the yield surface: (1) a concave-down yield surface as observed in clays and cohesive soils, and (2) a straight line shifted upward, i.e., a Coulomb strength envelope for cohesive materials, as observed in rocks.

V. SUMMARY AND DISCUSSION

In summary, by means of contact dynamics simulations, we investigated the stress-strain response of a cemented granular material subject to simple shear. For this purpose, we implemented a model of cementation between grains, as observed in soils and rocks. In this model cemented bonds are modeled as the combined effect of tensile strength, sliding friction, and rolling resistance; and their rupture leads to an irreversible loss of tensile strength and rolling resistance, turning the contact to purely frictional behavior. Two-dimensional polydisperse samples composed of 10 000 disks were constructed and then sheared in a simple shear numerical device. The macroscopic behavior of one of these samples was analyzed at initial yielding and after large cumulative shear strains, i.e., in the steady state.

We found that the cemented granular material exhibits two types of behavior depending on the magnitude of the applied stresses: (1) if the previously applied stresses have not damaged the cemented structure, the material behaves in a rigid-plastic fashion; and (2) if the previously applied stresses have damaged the cemented structure, the material's behavior approaches that of a loose cohesionless granular material. The yield stress states of the cemented granular material define a yield surface in the $(p^*:q^*)$ stress plane. This yield surface has a concave-down shape, as observed experimentally in clays and cemented soils [4,5,11]. This nonproportional behavior, typical of loose cohesive granular materials, results from the introduction of a local force scale, i.e., the tensile strength of the cemented bonds, and differs from that observed in cohesionless granular materials, for which the limit load surface is well described by a Coulomb strength envelope characterized by a single parameter: the angle of internal friction.

We also measured the direction of the plastic strains at initial yielding, showing that the material dilates when sheared at low confining stresses and contracts when sheared at high confining stresses. These results show that the dilatacy angle of cohesive granular media is not a material property but that it depends on the confining stress. The dilatancy angle of a cohesive granular material is independent of the stress level only in the limit of very dense packings.

In the elastoplastic models developed to represent the behavior of granular soils, it is convenient to assume that the material obeys the postulate of *normality*, which states that the plastic strain vectors are orthogonal to the yield surface. However, this hypothesis is inconsistent with experimental measurements (see, for example [11],) and simulations with

discrete element methods reported by Alonso-Marroquín *et al.* [33]. Our results agree with those presented by these authors. We found a deviation from normality of as much as 20° in the direction of the plastic strain vectors. Thus, for the granular material investigated here, the assumption of normality would lead to serious overestimations, i.e., greater than 20°, of the dilatancy angle $\psi=\sin^{-1}(\delta\varepsilon_p/\delta\varepsilon_q)$.

It was shown that, beyond yielding, the cemented structure gradually degrades until the material eventually behaves as a cohesionless material, whose shear strength is well described by a Coulomb law through an angle of internal friction. In this state, the strain concentrates inside a shear band whose thickness increases linearly with confinement until it eventually attains the thickness of the sample. When the confinement level tends to zero, the thickness of the shear band tends to a limit value of around 10 mean particle diameters. Our results at low confinement levels are thus reminiscent of those reported by Roscoe [34], stating that the thickness of the shear bands measured in sand samples is about $10\langle d\rangle$, and of the theoretical predictions reported by Mühlhaus and Vardoulakis [35] and by Bardet and Proubet [36], suggesting values varying from $15\langle d\rangle$ to $18\langle d\rangle$. We also measured the void ratio inside the shear band at the steady state, finding that it is a material property that only depends on contact parameters. This finding is in agreement with those reported by Desrues *et al.* [30], obtained from laboratory measurements, and with those reported by Rothenburg and Kruyt [37] and by Fazekas *et al.* [31], obtained from discrete element simulations. These findings, together with the dependence of the thickness of the shear band on the confining level, question the physical relevance of the void ratios obtained from global measurements in samples of granular materials with localized strain, e.g., in a soil sample with a shear band.

We studied the effect of the sample's compactness on the shape of the yield surface, showing that in the limit of a very dense material this surface approaches a straight line shifted upwards in the $(p^*:q^*)$ stress plane. This limit behavior corresponds to the Coulomb strength envelope for a cohesive material and can be characterized by two parameters: an angle of internal friction and a cohesive strength. This kind of behavior is consistent with a geometrical constraint imposed by the void ratio of the sample: a very dense granular material composed of rigid particles can hardly be compacted under isotropic compression, which implies that its yield stress under this load path would be infinite. Thus, our results show that the Coulomb strength envelope for cohesive granular materials is a particular case of a much broader picture and that the systematic application of this model can lead to serious misestimations of the material's strength.

It is evident that the behavior of a real cemented geomaterial is much more complex than that presented in this work. However, we think that some of the trends highlighted in this paper, as the effect of the void ratio on the shape of the yield surface, the non-normality of the plastic strains at yielding, and the effect of the confinement level on the thickness of the shear band, are robust features of the behavior of cohesive granular materials. For this reason, we think that the results presented here are relevant and can guide some of the choices to be made when implementing macroscopic constitutive models.

A natural extension of this work is a micromechanical description of the cemented material, in order to relate macroscopic yielding with local interactions. This study is presented in paper II. Another perspective is to determine the shape of the entire yield surface, as well as the effect of structural anisotropy and the degree of cementation on this surface. This must be carried out using a different shear device, like a biaxial device, capable of imposing stress paths such as isotropic compression and extension. The complete study of shear banding in this kind of systems is another question which merits further investigation. Some of these issues are being currently addressed and will be presented in a future paper.

ACKNOWLEDGMENTS

We warmly thank W. Fuentes for useful and stimulating discussions. This work was financially supported by the project Ecos Nord (Grant No. C08U01).

[1] J. K. Mitchell and K. Soga, *Fundamentals of Soil Behavior*, 3rd ed. (Wiley, New York, 2005).
[2] L. D. Wesley, Geotechnique **23**, 471 (1973).
[3] L. D. Wesley, Geotechnique **27**, 125 (1977).
[4] M. Maccarini, Ph.D. thesis, University of London, 1987.
[5] S. Leroueil and P. R. Vaughan, Geotechnique **40**, 467 (1990).
[6] L. D. Wesley, Geotechnique **51**, 901 (2001).
[7] A. Gens and R. Nova, in *Geotechnical Engineering of Hard Soils—Weak Rocks*, edited by A. Anagnostopoulos *et al.* (Balkema, Rotterdam, 1993), pp. 485–494.
[8] A. Vatsala, R. Nova, and B. R. S. Murthy, J. Geotech. Geoenviron. Eng. **127**, 679 (2001).
[9] R. Nova, R. Castellanza, and C. Tamagnini, Int. J. Numer. Analyt. Meth. Geomech. **27**, 705 (2003).
[10] A. Schofield and P. Wroth, *Critical State Soil Mechanics* (McGraw-Hill, New York, 1968).
[11] D. M. Wood, *Soil Behaviour and Critical State Soil Mechanics* (Cambridge, England, 1990).
[12] T. Gröger, U. Tüzün, and D. M. Heyes, Powder Technol. **133**, 203 (2003).
[13] V. Richefeu, M. S. El Youssoufi, and F. Radjaï, Phys. Rev. E **73**, 051304 (2006).
[14] V. Richefeu, M. S. El Youssoufi, E. Azéma, and F. Radjaï, Powder Technol. **190**, 258 (2009).
[15] S. Luding, Powder Technol. **158**, 45 (2005).
[16] F. A. Gilabert, J.-N. Roux, and A. Castellanos, Phys. Rev. E **75**, 011303 (2007).
[17] J.-Y. Delenne, M. S. E. Youssoufi, F. Cherblanc, and J.-C. Bénet, Int. J. Number. Analyt. Meth. Geomech. **28**, 1577 (2004).
[18] D. O. Potyondy and P. A. Cundall, Int. J. Rock Mech. Min. Sci. **41**, 1329 (2004).
[19] M. Jiang, S. Leroueil, and J.-M. Konrad, J. Eng. Mech. **131**,

1209 (2005).
[20] M. J. Jiang, H. S. Yu, and D. Harris, Int. J. Number. Analyt. Meth. Geomech. **30**, 723 (2006).
[21] A. Taboada, N. Estrada, and F. Radjaï, Phys. Rev. Lett. **97**, 098302 (2006).
[22] J. J. Moreau, Eur. J. Mech. A/Solids **13**, 93 (1994).
[23] M. Jean, *Mechanics of Geometrical Interfaces* (Elsevier, New York, 1995), pp. 463–486.
[24] M. Jean, Comput. Methods Appl. Mech. Eng. **177**, 235 (1999).
[25] M. Jean, *Micromécanique des Matériaux Granulaires* (Hermes, Paris, 2001), pp. 199–324.
[26] F. Radjai and V. Richefeu, Mech. Mater. **41**, 715 (2009).
[27] A. Taboada, K.-J. Chang, F. Radjai, and F. Bouchette, J. Geophys. Res. **110**, B09202 (2005).
[28] J. J. Moreau, *Friction, Arching, Contact Dynamics* (World Scientific, Singapore, 1997), pp. 233–247.
[29] L. Staron, F. Radjaï, and J.-P. Vilotte, Eur. Phys. J. E **18**, 311 (2005).
[30] J. Desrues, R. Chambon, M. Mokni, and F. Mazerolle, Geotechnique **46**, 529 (1996).
[31] S. Fazekas, J. Török, and J. Kertész, Phys. Rev. E **75**, 011302 (2007).
[32] GDR MiDi, Eur. Phys. J. E **14**, 341 (2004).
[33] F. Alonso-Marroquín, S. Luding, H. J. Herrmann, and I. Vardoulakis, Phys. Rev. E **71**, 051304 (2005).
[34] K. H. Roscoe, Geotechnique **20**, 129 (1970).
[35] H. B. Mühlhaus and I. Vardoulakis, Geotechnique **37**, 271 (1987).
[36] J. P. Bardet and J. Proubet, Geotechnique **41**, 599 (1991).
[37] L. Rothenburg and N. P. Kruyt, Int. J. Solids Struct. **41**, 5763 (2004).